ACS Catalysis

Research Article

Cite This: ACS Catal. 2019, 9, 4593–4599

pubs.acs.org/acscatalysis

ZnO As an Active and Selective Catalyst for Electrochemical Water Oxidation to Hydrogen Peroxide

Sara R. Kelly,[†,∇] Xinjian Shi,[‡,∇] Seoin Back,[†,∇,¶] Lauren Vallez,[‡] So Yeon Park,[‡,§] Samira Siahrostami,[*,†,∥] Xiaolin Zheng,[*,‡] and Jens K. Nørskov[*,†,⊥,#]

[†]SUNCAT Center for Interface Science and Catalysis, Department of Chemical Engineering, Stanford University, Stanford, California 94305, United States

[‡]Department of Mechanical Engineering, Stanford University, Stanford, California 94305, United States

[§]School of Advanced Materials Science & Engineering, Sungkyunkwan University, Suwon 16419, Republic of Korea

[∥]Department of Chemistry, University of Calgary, 2500 University Drive NW, Calgary, Alberta T2N 1N4, Canada

[⊥]SUNCAT Center for Interface Science and Catalysis, SLAC National Accelerator Laboratory, Menlo Park, California 94024, United States

[#]Department of Physics, Technical University of Denmark, Building 311, DK-2800 Lyngby, Denmark

Supporting Information

ABSTRACT: Electrochemical synthesis of hydrogen peroxide (H_2O_2) via two-electron water oxidation reaction (2e-WOR) is an ideal process for delocalized production for water cleaning and other applications. Previously reported water oxidation catalysts have limited activity and selectivity, imposing a bottleneck for broad adoption of this technology. We identify ZnO as a new stable, nontoxic, active, and selective catalyst for 2e-WOR to generate H_2O_2. Using density functional theory calculations, we propose that the $(10\bar{1}0)$ facet of ZnO is an effective catalyst for 2e-WOR and confirm the prediction experimentally. We synthesize ZnO nanoparticles with a high fraction of $(10\bar{1}0)$ facets and find that this catalyst gives an overpotential of 40 mV at 0.1 mA/cm^2 and peak Faradaic efficiency of 81% toward H_2O_2 evolution.

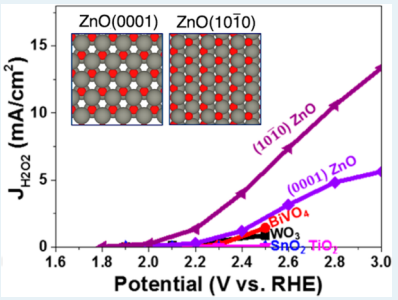

KEYWORDS: *water oxidation catalysis, hydrogen peroxide synthesis, zinc oxide, density functional theory, electrocatalysis*

1. INTRODUCTION

Potable water is vital for human life. Even though water resources are abundant on earth, <1% is accessible for human usage;[1] available resources are often contaminated by urban, industrial, and agricultural activities.[2] Many water pollutants need to be removed by total oxidation using an efficient and safe oxidizing agent.[3] Hydrogen peroxide (H_2O_2) is an elegant and green solution, capable of eliminating harmful bacteria, organic molecules, taste, and odor, leaving no residual behind. Moreover, it works over a wide pH range and can treat water with diverse quality. However, the cost and safety concerns related to H_2O_2 production and transportation are obstacles for its widespread application.

Direct thermocatalytic H_2O_2 synthesis from H_2 and O_2 is now well-described.[4,5] Electrochemical synthesis of H_2O_2 presents an alternative that has attracted much attention in recent years because an efficient process at ambient conditions combined with a cheap electricity source, including photovoltaics or wind, could provide an ideal process for decentralized production and applications.[6,7] Most studies have considered H_2O_2 production by reduction of O_2.[7−11] The oxidative process, while less studied in the literature, is particularly attractive due to its simplicity and the use of water as raw material. One major challenge is that the two-electron water oxidation reaction (2e-WOR) is only thermodynamically feasible at potentials above 1.76 V (at standard conditions). A limited number of catalyst materials are stable at such highly oxidizing conditions, and the competing 4-electron oxygen evolution reaction (OER) puts additional requirements on the catalyst in terms of selectivity toward H_2O_2 production. While many studies have sought to find efficient OER catalysts,[12−16] few have focused on the thermodynamically less-favorable 2e-WOR. Recent studies have demonstrated preferential 2e-WOR over several metal oxides such as MnO_x, TiO_2, $BiVO_4$, WO_3, SnO_2, Co_3O_4, and $CaSnO_3$.[17−20] These studies have shown that $CaSnO_3$ is the most active and selective electrocatalyst toward 2e-WOR.[21] However, $CaSnO_3$ is hazardous to the aquatic environment, and the experimentally measured limiting potential of $CaSnO_3$ is still higher than the theoretical best limiting potential U_L. Given the unique potential of 2e-WOR for ambient-condition onsite synthesis of H_2O_2, it is essential to identify a more efficient catalyst based on earth-abundant and nontoxic materials.

Received: December 5, 2018
Revised: March 26, 2019
Published: April 11, 2019

Downloaded via STANFORD UNIV on March 27, 2020 at 20:52:01 (UTC).
See https://pubs.acs.org/sharingguidelines for options on how to legitimately share published articles.

© 2019 American Chemical Society

DOI: 10.1021/acscatal.8b04873
ACS Catal. 2019, 9, 4593−4599

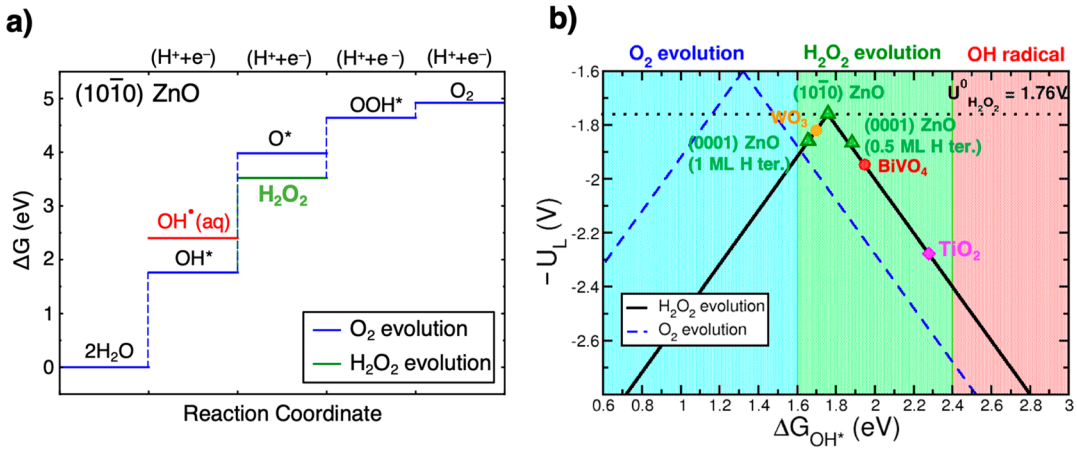

Figure 1. DFT calculation results of activity of (10$\bar{1}$0) and (0001) ZnO samples for O_2 and H_2O_2 evolution. (a) Free energy diagram of H_2O oxidation to $OH^•$ (red), H_2O_2 (green), and O_2 (blue) for the most active (10$\bar{1}$0) ZnO. (b) Volcano plots showing the calculated limiting potential U_L for four-electron H_2O oxidation to O_2 (blue dashed line) and two-electron H_2O oxidation to H_2O_2 (black solid line) as a function of OH* binding free energies (ΔG_{OH*}). The convention is such that a low value of U_L (a high value of $-U_L$) corresponds to a low overpotential and thus a high rate. The full lines correspond to the trend model described in the text, and DFT calculated values for different catalyst materials are included.[22] The 0.5 and 1 ML H ter. of (0001) ZnO indicate two different terminations at the bottom of the slabs.

In the present article, we use our previously developed theoretical model for catalytic activity and selectivity of the 2e-WOR to identify new catalysts.[22] The analysis predicts ZnO to be better in terms of overpotential and selectivity for H_2O_2 synthesis than known catalysts for the process and the (10$\bar{1}$0) facet to be the best. ZnO is a cheap, nontoxic material that has been known for centuries. It has been studied as a catalyst in photochemical production of H_2O_2[23,24] but to the best of our knowledge has not been studied for the 2e-WOR. We confirmed experimentally a remarkable activity and 2e-WOR selectivity compared to other reported metal oxide materials, as well as superior stability. In addition, we experimentally examined nanoparticles with different morphologies and identified the (10$\bar{1}$0) facet as especially promising. We devised a method for controlling which facet is dominating to produce the most effective 2e-WOR catalyst.

2. EXPERIMENTAL SECTION

2.1. Computational Details. We performed density functional theory (DFT) calculations using the Vienna Ab Initio Simulation Package (VASP)[25,26] with RPBE exchange-correlation functional[27] and projector augmented-wave (PAW) pseudopotential.[28] We noted that applying the Hubbard U correction results in weakening the calculated adsorption energies. However, the trends in activity remain unchanged.[29] The energy cutoff, a convergence criterion for self-consistent iteration, and geometry relaxation were set to 500 eV, 10^{-4} eV, and 0.05 eV/Å, respectively. Bulk ZnO in the most stable hexagonal wurtzite structure was fully relaxed using (10 × 10 × 6) Monkhorst pack k-points mesh, resulting in lattice parameters of a = 3.334 Å and c = 5.379 Å, which are in good agreement with the previous theoretical calculation and experiment.[30,31] Using the optimized unit cell, we modeled five layered ZnO (0001) and (10$\bar{1}$0) using (2 × 1) and (2 × 2) supercells, respectively, where the bottom three layers were kept fixed to the bulk positions. We added ∼15 Å of vacuum layer to avoid an imaginary interaction between repeating layers in z-direction. The ZnO(0001) facet is polar with inherent dipoles, which will cause an unphysical electron transfer to the atoms at the surface and affect the magnitude of DFT calculated adsorption energies. To quench the dipoles, we considered different hydrogen coverages (0, 0.5, and 1 ML) at the terminal oxygen atoms of the ZnO (0001) slab. This approach has been employed and validated in several previous reports.[30,32] Our results (summarized in Table S1) indicate that the effect of the hydrogen coverage between 0 and 0.5 ML is small, while that between 0.5 and 1 ML is significant. When we consider the solvation effect using VASPsol, the differences become more significant. However, we noted that the O-terminated (0001) surface is stable up to 0.5 ML of H*.[33,34] Thus, we used the calculated DFT result of 0.5 ML of H*. For comparison, we plotted the results of both 0.5 and 1 ML H* termination in Figure 1b.

Under the reaction conditions, surface Zn atoms may be precovered by oxygenated species such as O and OH depending on their reactivity, which then significantly affect the catalytic properties. Thus, we constructed the surface Pourbaix diagrams considering O* and OH* terminations on ZnO surfaces and determined the most stable surface coverage at 1.76 V_{RHE}, the equilibrium potential of H_2O/H_2O_2 (Supporting Information, Figure S1). On the basis of the determined most-stable surface coverage under the reaction conditions, we investigated free energetics along the reaction pathway of H_2O oxidation to H_2O_2.[19]

To convert calculated electronic energies into free energies, we added free energy corrections for adsorbates, which include zero-point energy, enthalpy, and entropy at 300 K using the harmonic oscillator approximation. For gaseous molecules, we used the ideal gas approximation with the partial pressure of 101 325 Pa for H_2 and 3 534 Pa for H_2O, which is the vapor pressure of H_2O. To avoid a poor description of a triplet O_2 molecule in RPBE, we used experimental formation free energies of H_2O and H_2O_2 as references. The effect of potential was included using the computational hydrogen electrode (CHE) method,[35] where the chemical potential of proton and electron pair equals to that of a half of hydrogen gas ($\mu(H^+ + e^-) = 1/2\ \mu(H_2)$) at standard conditions. As the potential is applied, the chemical potential of an electron is shifted by $-eU_{elec}$, where e and U_{elec} are elementary charge and electrode potential, respectively. To take into account the

DOI: 10.1021/acscatal.8b04873
ACS Catal. 2019, 9, 4593−4599

effect of solvation on free energetics, we employed an implicit solvation method (VASPsol)[36] as implemented in VASP, where the dielectric constant of the solvent was set to be 78.4 for water. This implicit solvation model yields calculated solvation energy of −0.17 eV for OH* adsorbate on ZnO $(10\bar{1}0)$ and −0.19 eV on ZnO (0001). This result agrees extremely well with the average calculated value of −0.19 eV for solvation energy of OH* across different oxides reported by Siahrostami and co-workers[37,38] using explicit solvent methods.

2.2. Synthesis of $(10\bar{1}0)$ ZnO Nanorods and (0001) ZnO Nanoparticles. For the synthesis of $(10\bar{1}0)$ ZnO nanorods on fluorine-doped tin oxide (FTO) substrates, the seed layer precursor was first prepared by dissolving 4.390 g of zinc acetate dehydrate $[Zn(CH_3COO)_2{\cdot}2H_2O]$ in 20 mL of 2-methoxyethanol and then adding an equal mole number of monoethanolamine (MEA). Next, the precursor solution was spin-coated on an FTO substrate. The spin-coating was conducted 3 times with an intermediate annealing step on a hot plate at 150 °C for 10 min and a final annealing in a box furnace at 350 °C for 30 min. The seed layer-coated FTO was placed in an autoclave (with the coating side facing the outside walls), which contained a mixture of 0.04 M zinc nitrate $(Zn(NO_3)_2{\cdot}6H_2O)$ and 0.04 M hexamethylenetetramine (HMT). The ZnO nanorod growth was carried out at 95 °C for 8 h. The obtained ZnO nanorod arrays were washed with deionized water and ethanol, dried in an oven at 60 °C overnight, and further annealed at 550 °C for 2 h.

For the synthesis of (0001) ZnO nanoparticles, a precipitate was first made and then deposited onto FTO. The precipitate solution was made by adding 5.268 g of $Zn(CH_3COO)_2{\cdot}2H_2O$ and 3.364 g of hexamethylenetetramine (HMTA) to a mixture of 32 mL of ethylene glycol (EG) and 8 mL of water in an autoclave. The autoclave was heated in an oven at 95 °C for 11 h. The obtained precipitate was rinsed with deionized water and ethanol thoroughly and dried at 60 °C overnight with additional annealing at 300 °C for 1 h. The ZnO precipitate was then collected and dispersed in isopropanol. The concentrations for both were kept at 0.3 mg/mL. After sonication for 2 h, the suspension was spin-coated on top of FTO glass using two steps, 500 rpm for 5 s and 2500 rpm for 20 s. The as-coated sample was dried at 150 °C for 10 min. This process was repeated 3 times for good coverage over FTO surface. Finally, the sample was annealed in a box furnace at 350 °C for 2 h to remove residue and for better attachment.

2.3. Electrochemical Performance Measurement for 2e-WOR. The electrochemical characterization methods for 2e-WOR were reported in detail previously.[19] Briefly, the catalytic performance was determined by using a potentiostat with the three-electrode system, in which ZnO/FTO was used as the working electrode, Ag/AgCl was used as the reference electrode, and carbon paper was used as the counter electrode. The electrolyte used was 2 M potassium bicarbonate. The Ag/AgCl reference electrode was calibrated by being placed in a pH = 0 solution (1 M H^+ H_2SO_4 solution) and connected with a Pt electrode with hydrogen gas purging the solution. The potential between Ag/AgCl and Pt electrodes was measured by a high-precision voltmeter, and this value is further used to calculate the experimental potential value vs RHE with additional considerations of the pH of the electrolyte (+0.0591 × pH). The error bars for electrochemical results are summarized from five independent measurements. The amount of generated H_2O_2 was detected by using H_2O_2 strips (Quantofix) with help from a strip reader (Macherey-Nagel Quantofix Relax Test Strip Reader). Here, after we applied the desired potential bias to the anode, we started to measure the H_2O_2 concentration every 20 min for 5 times. It should be noted that the measured H_2O_2 concentration is lower than what is being produced because H_2O_2 is unstable due to potential reduction to H_2O at the cathode or disproportionation reaction,[39] which may lead to underestimated Faraday efficiencies.

O_2 was detected by gas chromatography (GC) analysis. The FE for H_2O_2 production (%) is calculated using the following equation:

$$\mathrm{FE}(O_2 \text{ or } H_2O_2) = \frac{\text{amount of detected } O_2 \text{ or } H_2O_2 \text{ (mol)}}{\text{theoretical maximum } O_2 \text{ or } H_2O_2} \times 100\%$$

where the theoretical maximum amount of O_2 or H_2O_2 equals the total amount of electrons divided by four or two (in mol), respectively.

2.4. Other Measurements and Characterizations. The morphology of the samples was obtained using scanning electron microscopy (FEI XL30 Sirion SEM). The transmission electron microscopy (TEM) images were obtained by a transmission electron microscope (FEI Tecnai) equipped with a field-emission gun (FEG), scanning unit (STEM) with bright-field/dark-field detector, energy-dispersive X-ray spectroscopy (EDS) for compositional analysis, and charge-coupled device (CCD) camera. The crystalline information was obtained using the X-ray diffraction system with a Siemens diffractometer D500/5000 in the Bragg−Brentano geometry.

3. RESULTS AND DISCUSSION

3.1. Theoretical Analysis. Our theoretical analysis is based on understanding trends in free energy diagrams (FEDs) for the 4e-WOR (producing O_2), the 2e-WOR (producing H_2O_2), and the 1e-WOR (producing OH radicals).[19] Figure 1a shows a calculated FED for $(10\bar{1}0)$ ZnO based on a density functional calculation (see calculation details in Experimental Section and Supporting Information, Table S1), but the general model is not dependent on the electronic structure method used. The FED shows the energy of a set of intermediates leading to the three different products. We treat selectivity trends and activity trends separately. First, consider the question of selectivity. The free energy diagram illustrates that the thermodynamic driving force toward H_2O_2 is largest when (1) adsorbed O* is less stable than H_2O_2 in solution ($\Delta G_{O^*} < \Delta G_{H_2O_2}$(3.5 eV)) and (2) adsorbed OH* is more stable than OH radicals in solution $\Delta G_{OH^*} < \Delta G_{OH^\bullet}$. Point (1) means that H_2O_2 is produced instead of O* and (2) means that adsorbed OH does not readily desorb as a radical. Using the known scaling relation between the adsorption energy of O* and OH* ($\Delta G_{O^*} = 2\Delta G_{OH^*} + 0.28$),[40] the two conditions can be described by a single relation: 1.6 eV $\leq \Delta G_{OH^*} \leq$ 2.4 eV. Clearly, according to the calculations, ZnO $(10\bar{1}0)$ is in the right window for a high selectivity toward H_2O_2. Next, to understand catalytic activity, we use the limiting potential (U_L) as a measure of the rate—the lower the limiting potential, the higher is the rate. U_L is defined as the lowest potential at which all the elementary steps become thermoneutral,[17] and it has been shown to qualitatively agree with experimental onset potentials for oxygen electrochemistry.[19] Figure 1b combines the selectivity criterion and the

DOI: 10.1021/acscatal.8b04873
ACS Catal. 2019, 9, 4593−4599

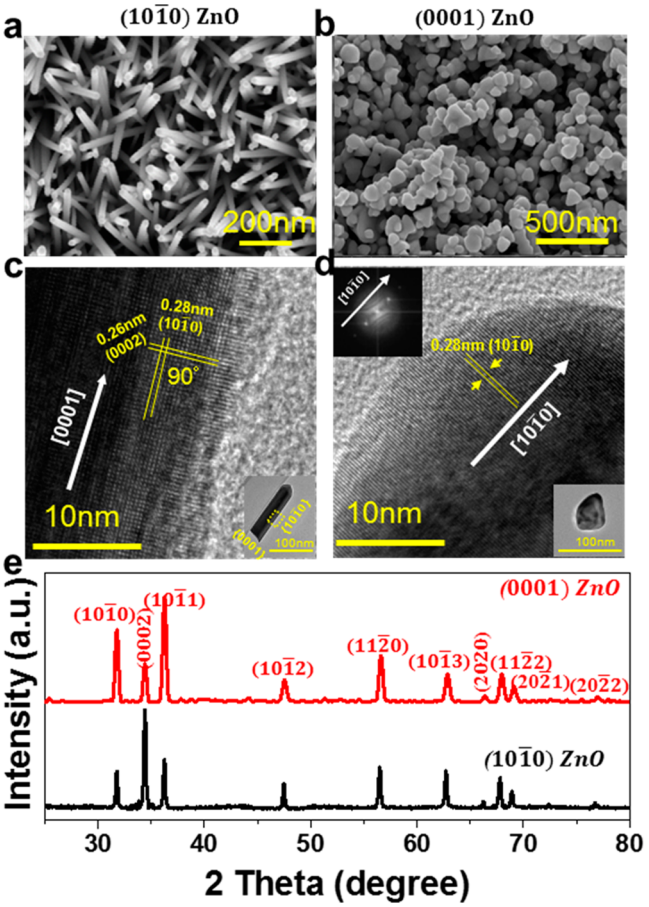

Figure 2. Morphology and crystallinity characterization of (10$\bar{1}$0) and (0001) ZnO samples. SEM images showing that (a) (10$\bar{1}$0) ZnO is composed of nanorods and (b) (0001) ZnO contains nanoparticles. TEM images showing that (c) (10$\bar{1}$0) and (d) (0001) ZnO grow along the [0001] and [10$\bar{1}$0] directions, respectively. (e) X-ray diffraction (XRD) spectra of both (10$\bar{1}$0) and (0001) ZnO, confirming the growth direction of TEM images.

activity measure in a single diagram. Materials in the green region should primarily produce H_2O_2, and the higher the value of $-U_L$, the higher the rate is expected to be. Clearly both the (10$\bar{1}$0) and (0001) facets of ZnO are predicted to be active and selective with (10$\bar{1}$0) ZnO near the top of the activity volcano and further away from the region of O_2 production than (0001) ZnO. Both should be more active than $BiVO_4$,[19] the hitherto best catalyst material.

3.2. Experimental Realization. To examine these theoretical predictions, we synthesized two ZnO samples on fluorine-doped tin oxide (FTO) substrates, each with a different dominant facet exposure. One has the facet (10$\bar{1}$0) exposed, while the other has dominant (0001) facet (see details in the Experimental Section); henceforth, there are referred to as (10$\bar{1}$0) and (0001) ZnO, respectively. Their morphologies are illustrated by the scanning electron microscopy (SEM) and high-resolution transmission electron microscopy (TEM) images in Figure 2a–d. The (10$\bar{1}$0) ZnO sample is composed of nanorods with an average diameter of 15–20 nm and length of ~150 nm. The (10$\bar{1}$0) ZnO sample has a growth direction of [0001], with a 90° angle between the (0002) facet and the (10$\bar{1}$0) facet, indicating the dominant exposed surface facet of (10$\bar{1}$0) (Figure 2c). This facet is also confirmed by a high-resolution TEM (HRTEM) image of the ZnO nanorod (Supporting Information, Figure S2a). In comparison, the (0001) ZnO sample is composed of nanoparticles with an average diameter of 45 nm (Figure 2b) with a [10$\bar{1}$0] growth direction (Figure 2d). Detailed TEM measurements show that the angle between two (10$\bar{1}$0) facets is 120° (Supporting Information, Figure S2b), indicating the exposed facet of (0001) for wurtzite ZnO. The X-ray diffraction (XRD) spectra in Figure 2e further confirm the growth direction of [0001] for (10$\bar{1}$0) ZnO and [10$\bar{1}$0] direction for (0001) ZnO, which is consistent with the HRTEM results.

Next, we compared the activity, selectivity, and stability of the two ZnO samples for the 2e-WOR for producing H_2O_2. The electrochemical performance was determined in a bicarbonate electrolyte using the standard three-electrode system, with ZnO/FTO as the working electrode, Ag/AgCl as the reference electrode, and carbon paper as the counter electrode. Figure 3a shows the current density and Faraday efficiency (FE) for H_2O_2 production as a function of the

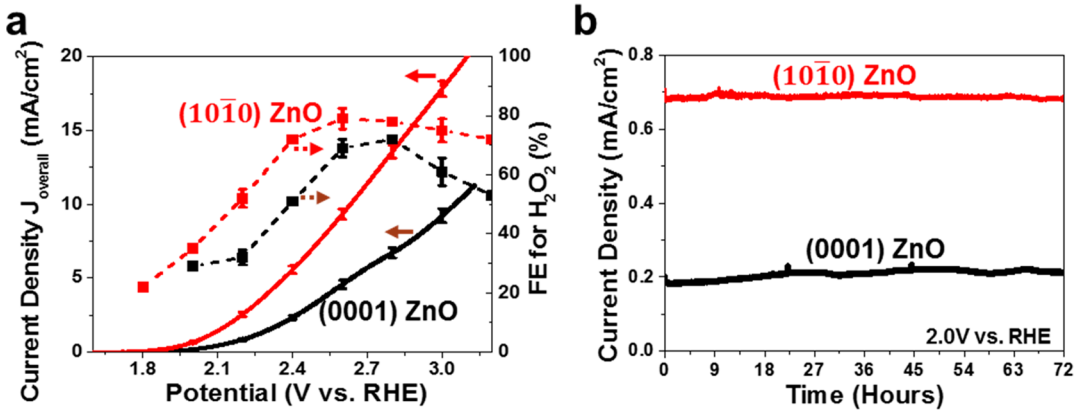

Figure 3. Comparison of the catalytic activity, selectivity, and stability of (10$\bar{1}$0) ZnO (red) and (0001) ZnO (black) for 2e-WOR toward H_2O_2 production. (a) Overall current density (solid lines) and FE of H_2O_2 (dash lines) vs applied bias. Experimental conditions: the $J-V$ curves were measured from 0.5 to 3.2 V with a scan rate of 50 mV/s in a three-electrode configuration, with catalyst on top of FTO as the working electrode, C paper as the counter electrode, and Ag/AgCl as the reference electrode. The electrolyte used was 2 M $KHCO_3$ without any gas purging (vol = 35 mL). The H_2O_2 concentration was measured every 20 min for 5 times under each bias, which was used to determine the error bar. (b) The 72 h stability test results for both (10$\bar{1}$0) ZnO and (0001) ZnO under 2.0 V vs RHE. The current densities were measured every 10 s.

DOI: 10.1021/acscatal.8b04873
ACS Catal. 2019, 9, 4593–4599

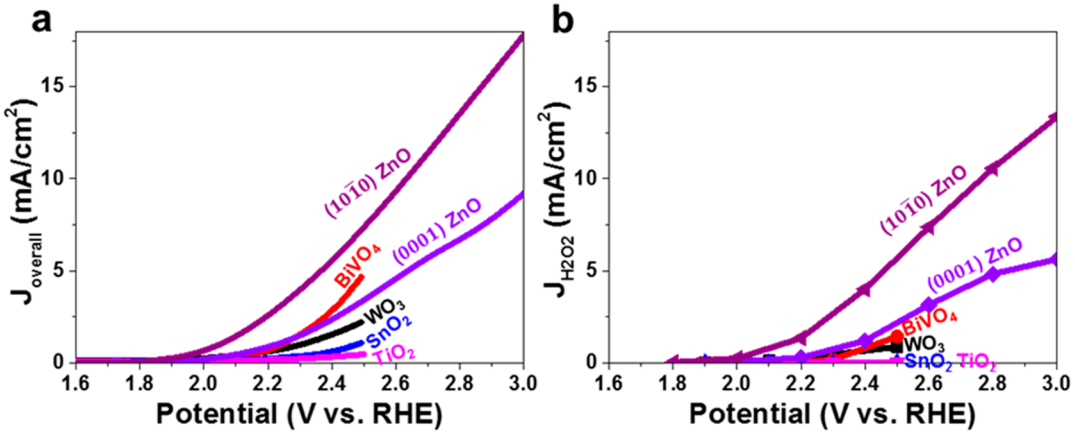

Figure 4. Comparison of the catalytic activity and selectivity of 2e-WOR H_2O_2 production. (a) Overall current density $J-V$ curves for (10$\bar{1}$0) ZnO, (0001) ZnO, and several reported metal oxides in ref 20. (b) Corresponding $J_{H_2O_2}-V$ curves for the current density toward the H_2O_2 formation, for which $J_{H_2O_2}$ was calculated by multiplying the overall current $J_{overall}$ with the Faraday efficiency at each potential. Experimental conditions for ZnO samples are the same as those shown in Figure 3.

applied potential. The (10$\bar{1}$0) ZnO sample has an earlier current onset and higher current density than those of (0001) ZnO. The (10$\bar{1}$0) ZnO sample achieves 0.1 mA/cm^2 at 1.80 V vs RHE, corresponding to an overpotential of 40 mV (the thermodynamic theoretical 2e-WOR potential is 1.76 V vs RHE).[22] It should be noted that the $J-V$ curve of (10$\bar{1}$0) ZnO shows negligible change after the iR correction (Supporting Information, Figure S4), indicating a small ohmic loss. Figure 3a further shows that (10$\bar{1}$0) ZnO has a higher FE for H_2O_2 than that of (0001) ZnO over the entire examined potential range. In addition, the FE of (10$\bar{1}$0) ZnO for H_2O_2 maintains a high value of 70% over a broad potential range (2.4−3.2 V vs RHE), and its peak value exceeds 80%. We have also measured the FE for O_2, and the sum of both FEs is ∼90−100% (Supporting Information, Figure S3), confirming the accuracy of the FE (H_2O_2) measurement. These experimental results support the theoretical predication that (10$\bar{1}$0) ZnO has better activity for 2e-WOR than (0001) ZnO. Finally, both (10$\bar{1}$0) and (0001) ZnO samples show stable performance under a constant bias of 2.0 V vs RHE for 72 h (Figure 3b), which is beneficial for on-site electrochemical synthesis of H_2O_2 for water treatment. In addition, the pH value of the electrolyte remains nearly the same, showing that bicarbonate is an effective buffer for at least 72 h.[41] Nevertheless, the long-term stability of ZnO and electrolyte can be different as ZnO can dissolve into zinc ions. In addition, over long periods of time, without CO_2 purging, gas evolution at the anode would remove dissolved CO_2, changing the electrolyte pH values. Such effects would compromise the long-term performance of the ZnO catalysts.

4. CONCLUSIONS

The present work highlights several interesting aspects. First of all, we have used a theoretical model to predict the activity and selectivity trends for the 2e-WOR, identifying a new catalyst, ZnO. We have also shown that the activity is facet-dependent and have devised a new synthesis method to exploit such dependence. To the best of our knowledge, we have achieved the best performance of 2e-WOR to date with ZnO, as reflected by the comparisons of the total current density $J-V$ curves (Figure 4a), the calculated current density toward H_2O_2 formation (Figure 4b), and the Faraday efficiencies at 3.0 V vs RHE (Figure 5) of various electrocatalysts reported here and in previous studies.[18,19] These comparisons reveal that both (10$\bar{1}$0) and (0001) ZnO are generally good H_2O_2 catalysts for 2e-WOR, with (10$\bar{1}$0) ZnO being the best to date. Given the unmatched electrocatalytic performance, low cost, and non-toxicity of ZnO, this work demonstrates a very attractive catalyst for on-site production of H_2O_2 from WOR. Toward this goal, further research is needed to test ZnO for potential commercial use of H_2O_2 production, its durability under light for even lower-bias H_2O_2 production, the stability of H_2O_2 generated in this system, the system level of optimization, and testing with different types of water.

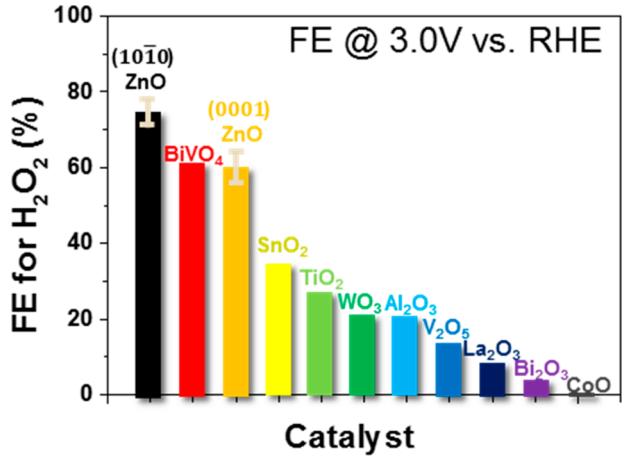

Figure 5. Faraday efficiency (FE) at 3.0 V vs RHE for (10$\bar{1}$0) ZnO, (0001) ZnO, and several reported metal oxides in refs 18 and 19. $BiVO_4$, SnO_2, and WO_3 are from ref 19, and the others are from ref 18 (@ 3.0 V under two-electrode system). The FE of ZnO samples is extracted from the results in Figure 3a. The error bars represent the FE range from 5 independent measurements.

■ ASSOCIATED CONTENT

Supporting Information

The Supporting Information is available free of charge on the ACS Publications website at DOI: 10.1021/acscatal.8b04873.

Surface Pourbaix digrams of ZnO (0001) and (10$\bar{1}$0) and the calculated binding free energies, HRTEM

DOI: 10.1021/acscatal.8b04873
ACS Catal. 2019, 9, 4593−4599

images, Faradaic efficiencies, and current−potential (*J*−*V*) curves (PDF)

AUTHOR INFORMATION

Corresponding Authors

*E-mail: samira.siahrostami@ucalgary.ca.
*E-mail: xlzheng@stanford.edu.
*E-mail: jkno@dtu.dk.

ORCID

Sara R. Kelly: 0000-0001-9424-2489
Seoin Back: 0000-0003-4682-0621
So Yeon Park: 0000-0001-6774-0941
Samira Siahrostami: 0000-0002-1192-4634
Xiaolin Zheng: 0000-0002-8889-7873

Present Address

[¶]Department of Chemical Engineering, Carnegie Mellon University, Pittsburgh, PA, USA

Author Contributions

[▽]S.R.K., X.S., and S.B. contributed equally.

Notes

The authors declare no competing financial interest.

ACKNOWLEDGMENTS

This work was supported by the U.S. Department of Energy, Office of Science, Office of Basic Energy Science, via Grant DE-SC0008685 to the SUNCAT Center of Interface Science and Catalysis. X.Z. thanks the generous support of the Stanford Woods Institute for the Environment and the Stanford Natural Gas Initiative.

REFERENCES

(1) Oki, T.; Kanae, S. Global hydrological cycles and world water resources. *Science* **2006**, *313* (5790), 1068−1072.

(2) Carpenter, S. R.; Caraco, N. F.; Correll, D. L.; Howarth, R. W.; Sharpley, A. N.; Smith, V. H. Nonpoint pollution of surface waters with phosphorus and nitrogen. *Ecological applications* **1998**, *8* (3), 559−568.

(3) Shannon, M. A.; Bohn, P. W.; Elimelech, M.; Georgiadis, J. G.; Marinas, B. J.; Mayes, A. M. Science and technology for water purification in the coming decades. In *Nanoscience And Technology: A Collection of Reviews from Nature Journals*; World Scientific: 2010; pp 337−346.

(4) Alba-Rubio, A.; Plauck, A.; Stangland, E.; Mavrikakis, M.; Dumesic, J. Direct Synthesis of Hydrogen Peroxide Over Au-Pd Catalysts Prepared by Electroless Deposition. *Catal. Lett.* **2015**, *145* (12), 2057−2065.

(5) Edwards, J.; Solsona, B.; N, E.; Carley, A.; Herzing, A.; Kiely, C.; Hutchings, G. Switching Off Hydrogen Peroxide Hydrogenation in the Direct Synthesis Process. *Science* **2009**, *323* (5917), 1037−1041.

(6) Viswanathan, V.; Hansen, H. A.; Rossmeisl, J.; Norskov, J. K. Unifying the $2e^-$ and $4e^-$ reduction of oxygen on metal surfaces. *J. Phys. Chem. Lett.* **2012**, *3* (20), 2948−2951.

(7) Siahrostami, S.; Verdaguer-Casadevall, A.; Karamad, M.; Deiana, D.; Malacrida, P.; Wickman, B.; Escudero-Escribano, M.; Paoli, E. A.; Frydendal, R.; Hansen, T. W.; et al. Enabling direct H_2O_2 production through rational electrocatalyst design. *Nat. Mater.* **2013**, *12* (12), 1137−1143.

(8) Verdaguer-Casadevall, A.; Deiana, D.; Karamad, M.; Siahrostami, S.; Malacrida, P.; Hansen, T. W.; Rossmeisl, J.; Chorkendorff, I.; Stephens, I. E. Trends in the electrochemical synthesis of H_2O_2: enhancing activity and selectivity by electrocatalytic site engineering. *Nano Lett.* **2014**, *14* (3), 1603−1608.

(9) Chen, S.; Chen, Z.; Siahrostami, S.; Higgins, D.; Nordlund, D.; Sokaras, D.; Kim, T. R.; Liu, Y.; Yan, X.; Nilsson, E. Designing Boron Nitride Islands in Carbon Materials for Efficient Electrochemical Synthesis of Hydrogen Peroxide. *J. Am. Chem. Soc.* **2018**, *140*, 7851−7859.

(10) Chen, S.; Chen, Z.; Siahrostami, S.; Kim, T. R.; Nordlund, D.; Sokaras, D.; Nowak, S.; To, J. W.; Higgins, D.; Sinclair, R.; et al. Defective Carbon-Based Materials for the Electrochemical Synthesis of Hydrogen Peroxide. *ACS Sustainable Chem. Eng.* **2018**, *6* (1), 311−317.

(11) Yang, S.; Verdaguer-Casadevall, A.; Arnarson, L.; Silvioli, L.; Čolić, V.; Frydendal, R.; Rossmeisl, J.; Chorkendorff, I.; Stephens, I. E. Toward the Decentralized Electrochemical Production of H_2O_2: A Focus on the Catalysis. *ACS Catal.* **2018**, *8* (5), 4064−4081.

(12) Hong, W.; Risch, M.; Stoerzinger, K.; Grimaud, A.; Suntivich, J.; Shao-Horn, Y. Toward the rational design of non-precious transition metal oxides for oxygen electrocatalysis. *Energy Environ. Sci.* **2015**, *8* (5), 1404−1427.

(13) Louie, M.; Bell, A. An Investigation of Thin-Film Ni-Fe Oxide Catalysts for the Electrochemical Evolution of Oxygen. *J. Am. Chem. Soc.* **2013**, *135* (33), 12329−12337.

(14) Man, I. C.; Su, H. Y.; Calle-Vallejo, F.; Hansen, H. A.; Martínez, J. I.; Inoglu, N. G.; Kitchin, J.; Jaramillo, T. F.; Norskov, J. K.; Rossmeisl, J. Universality in oxygen evolution electrocatalysis on oxide surfaces. *ChemCatChem* **2011**, *3* (7), 1159−1165.

(15) Zhang, B.; Zheng, X.; Voznyy, O.; Comin, R.; Bajdich, M.; García-Melchor, M.; Han, L.; Xu, J.; Liu, M.; Zheng, L.; García de Arquer, F. P.; Dinh, C.; Fan, F.; Yuan, M.; Yassitepe, E.; Chen, N.; Regier, T.; Liu, P.; Li, Y.; De Luna, P.; Janmohamed, A.; Xin, H.; Yang, H.; Vojvodic, A.; Sargent, E. H. Homogeneously dispersed multimetal oxygen-evolving catalysts. *Science* **2016**, *352* (6283), 333−337.

(16) Gerken, J. B.; McAlpin, J. G.; Chen, J. Y.; Rigsby, M. L.; Casey, W. H.; Britt, R. D.; Stahl, S. S. Electrochemical water oxidation with cobalt-based electrocatalysts from pH 0−14: the thermodynamic basis for catalyst structure, stability, and activity. *J. Am. Chem. Soc.* **2011**, *133* (36), 14431−14442.

(17) Viswanathan, V.; Hansen, H. A.; Norskov, J. K. Selective electrochemical generation of hydrogen peroxide from water oxidation. *J. Phys. Chem. Lett.* **2015**, *6* (21), 4224−4228.

(18) Fuku, K.; Miyase, Y.; Miseki, Y.; Gunji, T.; Sayama, K. Enhanced oxidative hydrogen peroxide production on conducting glass anodes modified with metal oxides. *ChemistrySelect* **2016**, *1* (18), 5721−5726.

(19) Shi, X.; Siahrostami, S.; Li, G.-L.; Zhang, Y.; Chakthranont, P.; Studt, F.; Jaramillo, T. F.; Zheng, X.; Norskov, J. K. Understanding activity trends in electrochemical water oxidation to form hydrogen peroxide. *Nat. Commun.* **2017**, *8* (1), 701.

(20) Zhang, J.; Chang, X.; Luo, Z.; Wang, T.; Gong, J. A Highly Efficient Photoelectrochemical H_2O_2 Production Reaction with Co_3O_4 as Co-catalysts. *Chem. Commun.* **2018**, *54*, 7026−7029.

(21) Park, S. Y.; Abroshan, H.; Shi, X.; Jung, H. S.; Siahrostami, S.; Zheng, X. $CaSnO_3$: An Electrocatalyst for 2-Electron Water Oxidation Reaction to Form H_2O_2. *ACS Energy Letters* **2019**, *4*, 352−357.

(22) Siahrostami, S.; Li, G.-L.; Viswanathan, V.; Norskov, J. K. One- or two-electron water oxidation, hydroxyl radical, or H_2O_2 evolution. *J. Phys. Chem. Lett.* **2017**, *8* (6), 1157−1160.

(23) Rubin, T. R.; Calvert, J. G.; Rankin, G. T.; MacNevin, W. Photochemical Synthesis of Hydrogen Peroxide at Zinc Oxide Surfaces1. *J. Am. Chem. Soc.* **1953**, *75* (12), 2850−2853.

(24) Domènech, X.; Ayllón, J. A.; Peral, J. H_2O_2 formation from photocatalytic processes at the ZnO/water interface. *Environ. Sci. Pollut. Res.* **2001**, *8* (4), 285−287.

(25) Kresse, G.; Joubert, D. From ultrasoft pseudopotentials to the projector augmented-wave method. *Phys. Rev. B: Condens. Matter Mater. Phys.* **1999**, *59* (3), 1758.

(26) Kresse, G.; Furthmüller, J. Efficiency of ab-initio total energy calculations for metals and semiconductors using a plane-wave basis set. *Comput. Mater. Sci.* **1996**, *6* (1), 15−50.

(27) Hammer, B.; Hansen, L. B.; Norskov, J. K. Improved adsorption energetics within density-functional theory using revised

DOI: 10.1021/acscatal.8b04873
ACS Catal. 2019, 9, 4593−4599

Perdew–Burke–Ernzerhof functionals. *Phys. Rev. B: Condens. Matter Mater. Phys.* **1999**, *59* (11), 7413–7421.
(28) Blöchl, P. E. Projector augmented-wave method. *Phys. Rev. B: Condens. Matter Mater. Phys.* **1994**, *50* (24), 17953.
(29) Xu, Z.; Rossmeisl, J.; Kitchin, J. R. A linear response DFT+U study of trends in the oxygen evolution activity of transition metal rutile dioxides. *J. Phys. Chem. C* **2015**, *119* (9), 4827–4833.
(30) Medford, A. J.; Sehested, J.; Rossmeisl, J.; Chorkendorff, I.; Studt, F.; Norskov, J. K.; Moses, P. G. Thermochemistry and microkinetic analysis of methanol synthesis on ZnO (0 0 0 1). *J. Catal.* **2014**, *309*, 397–407.
(31) Escudero, R.; Escamilla, R. Ferromagnetic behavior of high-purity ZnO nanoparticles. *Solid State Commun.* **2011**, *151* (2), 97–101.
(32) Wöll, C. The chemistry and physics of zinc oxide surfaces. *Prog. Surf. Sci.* **2007**, *82* (2–3), 55–120.
(33) Meyer, B. First-principles study of the polar O-terminated ZnO surface in thermodynamic equilibrium with oxygen and hydrogen. *Phys. Rev. B: Condens. Matter Mater. Phys.* **2004**, *69* (4), 045416.
(34) Kresse, G.; Dulub, O.; Diebold, U. Competing stabilization mechanism for the polar ZnO (0001)-Zn surface. *Phys. Rev. B: Condens. Matter Mater. Phys.* **2003**, *68* (24), 245409.
(35) Norskov, J. K.; Rossmeisl, J.; Logadottir, A.; Lindqvist, L.; Kitchin, J. R.; Bligaard, T.; Jonsson, H. Origin of the overpotential for oxygen reduction at a fuel-cell cathode. *J. Phys. Chem. B* **2004**, *108* (46), 17886–17892.
(36) Mathew, K.; Sundararaman, R.; Letchworth-Weaver, K.; Arias, T.; Hennig, R. G. Implicit solvation model for density-functional study of nanocrystal surfaces and reaction pathways. *J. Chem. Phys.* **2014**, *140* (8), 084106.
(37) Siahrostami, S.; Vojvodic, A. Influence of adsorbed water on the oxygen evolution reaction on oxides. *J. Phys. Chem. C* **2015**, *119* (2), 1032–1037.
(38) Gauthier, J. A.; Dickens, C. F.; Chen, L. D.; Doyle, A. D.; Norskov, J. K. Solvation effects for oxygen evolution reaction catalysis on IrO_2 (110). *J. Phys. Chem. C* **2017**, *121* (21), 11455–11463.
(39) Jaouen, F.; Dodelet, J.-P. O_2 reduction mechanism on non-noble metal catalysts for PEM fuel cells. Part I: experimental rates of O_2 electroreduction, H_2O_2 electroreduction, and H_2O_2 disproportionation. *J. Phys. Chem. C* **2009**, *113* (34), 15422–15432.
(40) García-Mota, M.; Vojvodic, A.; Metiu, H.; Man, I. C.; Su, H. Y.; Rossmeisl, J.; Norskov, J. K. Tailoring the Activity for Oxygen Evolution Electrocatalysis on Rutile TiO_2 (110) by Transition-Metal Substitution. *ChemCatChem* **2011**, *3* (10), 1607–1611.
(41) Liu, C.-F.; Lu, Y.-J.; Hu, C.-C. Effects of anions and pH on the stability of ZnO nanorods for photoelectrochemical water splitting. *ACS Omega* **2018**, *3* (3), 3429–3439.

DOI: 10.1021/acscatal.8b04873
ACS Catal. 2019, 9, 4593–4599